

AD _____

Award Number: DAMD17-97-1-7304

TITLE: Simulation, Measurements and Image Processing for Capillary
Optical Digital Mammography (96 Breast)

PRINCIPAL INVESTIGATOR: Hui Wang

CONTRACTING ORGANIZATION: State University of New York at Albany
Albany, New York 12222

REPORT DATE: September 1999

TYPE OF REPORT: Annual

PREPARED FOR: U.S. Army Medical Research and Materiel Command
Fort Detrick, Maryland 21702-5012

DISTRIBUTION STATEMENT: Approved for public release
distribution unlimited

The views, opinions and/or findings contained in this report are those of the author(s) and should not be construed as an official Department of the Army position, policy or decision unless so designated by other documentation.

20010608 040

REPORT DOCUMENTATION PAGE

Form Approved
OMB No. 074-0188

Public reporting burden for this collection of information is estimated to average 1 hour per response, including the time for reviewing instructions, searching existing data sources, gathering and maintaining the data needed, and completing and reviewing this collection of information. Send comments regarding this burden estimate or any other aspect of this collection of information, including suggestions for reducing this burden to Washington Headquarters Services, Directorate for Information Operations and Reports, 1215 Jefferson Davis Highway, Suite 1204, Arlington, VA 22202-4302, and to the Office of Management and Budget, Paperwork Reduction Project (0704-0188), Washington, DC 20503

1. AGENCY USE ONLY (Leave blank)		2. REPORT DATE September 1999		3. REPORT TYPE AND DATES COVERED Annual (01 Sep 98 - 31 Aug 99)	
4. TITLE AND SUBTITLE Simulation, Measurements and Image Processing for Capillary Optical Digital Mammography (96 Breast)				5. FUNDING NUMBERS DAMD17-97-1-7304	
6. AUTHOR(S) Hui Wang					
7. PERFORMING ORGANIZATION NAME(S) AND ADDRESS(ES) Stae University of New York at Albany Albany, New York 12222 e-mail: hw7123@cnsunix.albany.edu				8. PERFORMING ORGANIZATION REPORT NUMBER	
9. SPONSORING / MONITORING AGENCY NAME(S) AND ADDRESS(ES) U.S. Army Medical Research and Materiel Command Fort Detrick, Maryland 21702-5012				10. SPONSORING / MONITORING AGENCY REPORT NUMBER	
11. SUPPLEMENTARY NOTES					
12a. DISTRIBUTION / AVAILABILITY STATEMENT Approved for public release Distribution unlimited				12b. DISTRIBUTION CODE	
13. ABSTRACT (Maximum 200 Words) Capillary optics, which use total external reflection to transmit x rays, have been proved to have great advantages in scatter reduction and resolution improvement in mammography application. The purpose of the proposed work is to perform lens simulation and image artifact elimination as part of the work of capillary optical mammography research. A lens simulation extended from the previous single fiber simulation has been implemented, a lens for the protocol mammography system has been re-measured in an extended energy range and analyzed with the program. The simulation has been proved to be helpful in understanding the lens performance. Modulation Transfer Function (MTF) is the most fundamental measurement of spatial resolution used in radiology. Non-uniform transmission introduces difficulties in MTF measurement. A method to measure MTF by taking an edge image and processed with background reduction technique has been developed. The modeling capability has been extended and has lead to a real development of understanding of the nature of polycapillary defects, which is already leading to improvements in the manufacturing processes. Further, the increased confidence in the modeling allows future lens geometries to be effectively "tested" in simulation so that design parameters can be rapidly optimized.					
14. SUBJECT TERMS Breast Cancer				15. NUMBER OF PAGES 31	
				16. PRICE CODE	
17. SECURITY CLASSIFICATION OF REPORT Unclassified	18. SECURITY CLASSIFICATION OF THIS PAGE Unclassified	19. SECURITY CLASSIFICATION OF ABSTRACT Unclassified		20. LIMITATION OF ABSTRACT Unlimited	

NSN 7540-01-280-5500

Standard Form 298 (Rev. 2-89)
Prescribed by ANSI Std. Z39-18
298-102

FOREWORD

Opinions, interpretations, conclusions and recommendations are those of the author and are not necessarily endorsed by the U.S. Army.

____ Where copyrighted material is quoted, permission has been obtained to use such material.

____ Where material from documents designated for limited distribution is quoted, permission has been obtained to use the material.

____ Citations of commercial organizations and trade names in this report do not constitute an official Department of Army endorsement or approval of the products or services of these organizations.

____ In conducting research using animals, the investigator(s) adhered to the "Guide for the Care and Use of Laboratory Animals," prepared by the Committee on Care and use of Laboratory Animals of the Institute of Laboratory Resources, national Research Council (NIH Publication No. 86-23, Revised 1985).

____ For the protection of human subjects, the investigator(s) adhered to policies of applicable Federal Law 45 CFR 46.

____ In conducting research utilizing recombinant DNA technology, the investigator(s) adhered to current guidelines promulgated by the National Institutes of Health.

____ In the conduct of research utilizing recombinant DNA, the investigator(s) adhered to the NIH Guidelines for Research Involving Recombinant DNA Molecules.

____ In the conduct of research involving hazardous organisms, the investigator(s) adhered to the CDC-NIH Guide for Biosafety in Microbiological and Biomedical Laboratories.

Carolyn McDonald 9/29/99
PI - Signature Date

4. Table of Contents

1. Front Cover.....	1
2. Report Document Page	2
3 Foreword	3
4. Table of Contents	4
5. Introduction.....	5
6. Body	6
6.1. DEffect Simulation	6
6.2. Simulation of Multifiber Optics.....	15
6.3. Magnifying Linear Monolithic Antiscatter Optics	16
6.3.1. Transmission	16
6.3.2. Simulations.....	18
6.3.3. Potential for Lead Glass	20
6.3.4. MTF Calculation	24
7. Key Research Accomplishments	28
8. Reportable Outcomes.....	28
8.1. Manuscripts.....	28
8.2. Presentations	29
8.3. Poster Presentations.....	29
8.4. Employment/Research Received.....	29
8.4.1. Research Employment	29
9. Conclusions	29
10. References	30

5. Introduction

At the present time the best way to fight breast cancer is through early detection. The size of malignancies in the early stage is very small, and the absorption of x rays by the malignancies and the breast tissue is similar. Thus high contrast and good resolution are especially important in mammography. In current digital mammography systems, contrast loss occurs from scattered x rays that strike the detector from all directions, and resolution is limited by the pixel size of the digital detector for computed radiography phosphor plates (CR plates), or the conversion efficiency and total number of pixels for visible light CCD systems.

Capillary x-ray optics use total external reflection to guide x rays through tiny hollow glass tubes, similar to the way conventional fiber optics transmit light. A capillary lens is a bundle of hollow glass tubes with channel sizes as small as few microns. The critical angle for total external reflection is as small as a few mrad (1.5mrad for 20 keV photons).^{1,2} A capillary lens can provide almost total scatter rejection. A well-designed lens can also provide magnification without image degradation from a finite source spot size. Thus the effective resolution can be improved while a CR plate is used. Capillary optics can also demagnify the image to match a direct area detector, such as a CZT detector^{3,4}, which maybe available in the

near future. Unlike the fiber-optic-CCD combination, this system does not involve the use of a phosphor to convert the x rays to visual light. The solid state detector can provide almost 100% quantum efficiency.

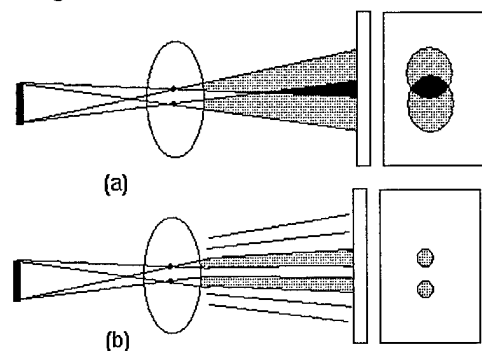


Figure 1 a) Image blurring in normal airgap magnification. b) Capillary lens between the patient and detector eliminates the focus

Capillary optical mammography has been cooperatively investigated by Center for X-ray Optics at University at Albany and the Radiology Dept. of University of Wisconsin for many years. Previous work has demonstrated the bright future of capillary optics in digital mammography with both contrast and resolution improvement.^{5,6} Among the problems found in the previous work are the small size of the lens and non-uniform transmission. Artifacts caused by non-uniformity of transmission were observed in the image. Eliminating artifacts by image processing may be a better and more economic way than fabricating an ideal lens. Low

reproducibility can be a problem in lens manufacture. It is extremely important to design a large lens by combining several small pieces. So a better understanding of lens behavior is necessary. Theoretical simulation has been proved to be very helpful in understanding the capillary and lens behavior, and provide feedback to the manufacturing process.^{Error! Bookmark not defined.} It would also be easier to manufacture large lenses if they were shorter; for that reason, lead glass optics, which would stop scattered radiation with a shorter length, were investigated.

The proposed work is focused on lens measurements, computer simulations and image processing. During the first year of the work, a lens simulation has been developed and applied to the experimental data. The simulation has proved to be helpful to understand the lens behavior. MTF is usually measured by taking an image of a slit. It is difficult to measure a stationary lens with this method when the transmission of the lens is not uniform. A method to measure MTF by taking an edge image was developed with background deduction technique. The lens simulation was expanded in the second year, and lead glass optics were investigated. During the second year, the principal investigator was changed from Dr. Lei Wang to Dr. Hui Wang.

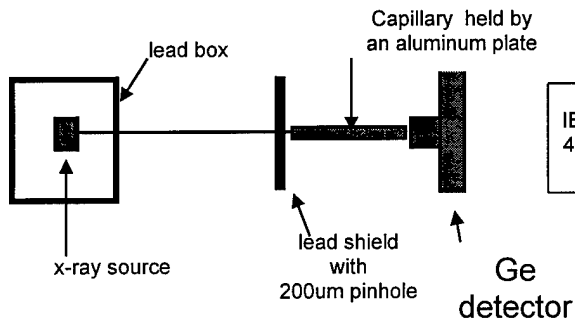


Figure 2. Experimental setup.

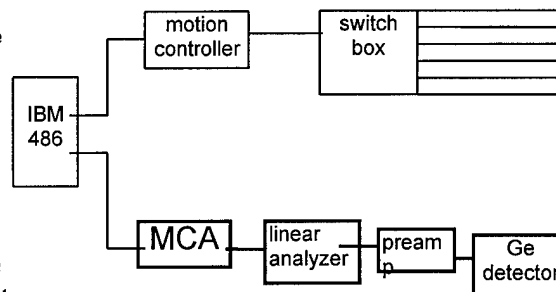


Figure 3. Electronic system.

6. Body

6.1. DEFECT SIMULATION

An important step in optics development was the breakthrough in modeling capacity, which has led to an unprecedented level of theoretical understanding of the basic properties of polycapillary fibers, especially fiber defects. To evaluate the experimental performance of polycapillary fibers, and design capillary optics, it is necessary to be able to predict theoretical behavior for complex geometries. The modeling program for single fibers is based on a Monte Carlo simulation of simple geometrical optics. The computational speed is greatly enhanced by a reduction to two dimensions by projecting the trajectory onto the local fiber cross-section.⁷ Reflectivities are computed from standard tables.⁸ Significant recent progress has been made in understanding the effect of capillary profile error, waviness, and roughness on the transmission spectra.⁹ This is extremely important in providing feedback to the manufacturing process. It has been found that extremely good fits can be produced with only two fitting parameters if a more physical model of waviness is employed.¹⁰

The experimental arrangement for single capillary measurements is shown in Figure 2 and Figure 4. An optical rail affixed to an optical table carries an x-ray source, fiber platform, and x-ray detector. Each can be positioned independently in three

Type	Description	Outer Diameter, mm	Channel Size, μm	Open Area	Length, mm
A	Borosilicate	0.5	12	65%	105
B	Lead glass	0.5	12	52%	95
C	Borosilicate	0.75	22	50%	136
D	Borosilicate	4	12	55%	130
E	Borosilicate	0.3	4-5	55%	105

Table 1. Description of polycapillary fibers.

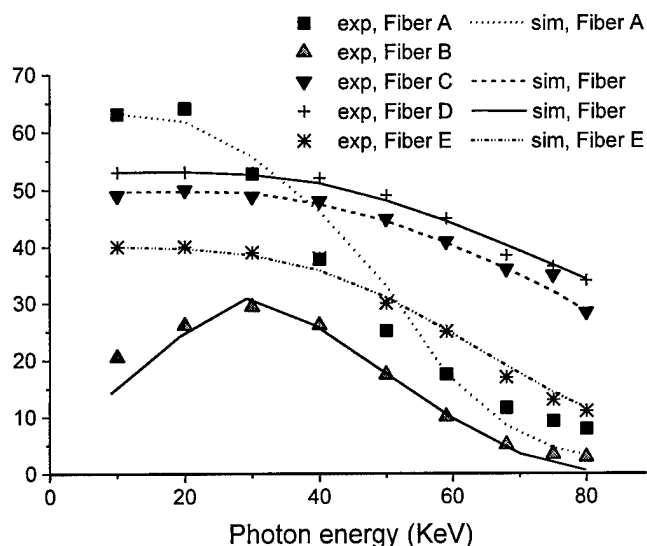


Figure 4. Measured transmission versus energy for polycapillary fibers listed in Table 1.

transmission expected for a linear capillary optic employed as an antiscatter grid. The transmission falls off at higher energies. Modeling this transmission spectra has lead to a greater understanding of defects in polycapillary optics.

In Figure 5, simulations with or without roughness corrections are compared with the experimental data. In these measurements the source is scanned transverse to the fiber axis. The simulation with a roughness height of 0.5 nm fits the experimental data quite well. It is definitely over-corrected when the roughness is 1.0 nm. The same simulations, shown in Figure 7, are also carried out at 68 keV, where the width of the curve is narrower than that at 10 keV because of the smaller critical angle. As a result,

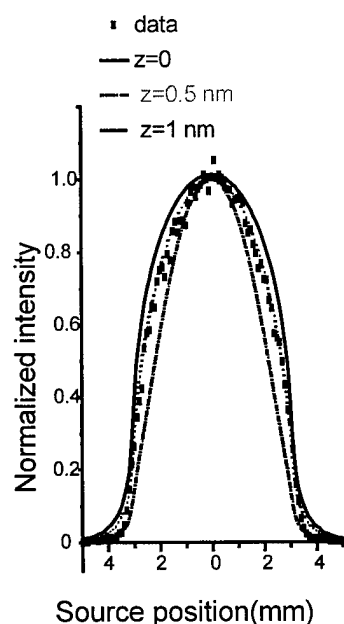


Figure 5. Source scans at 10 keV.

dimensions. A collimator is placed before the fiber and any remaining x-ray leakage around the fiber is eliminated with metal powder or filings. The measured fibers are described in Table 1.

The results of transmission studies as a function of photon energy are shown in Figure 4.^{11,12} All of the fibers except the lead glass have transmissions at 20 keV nearly equal to their fractional open area (the fraction of the cross section of the capillary which is open space, the rest being glass walls). This transmission corresponds to the primary

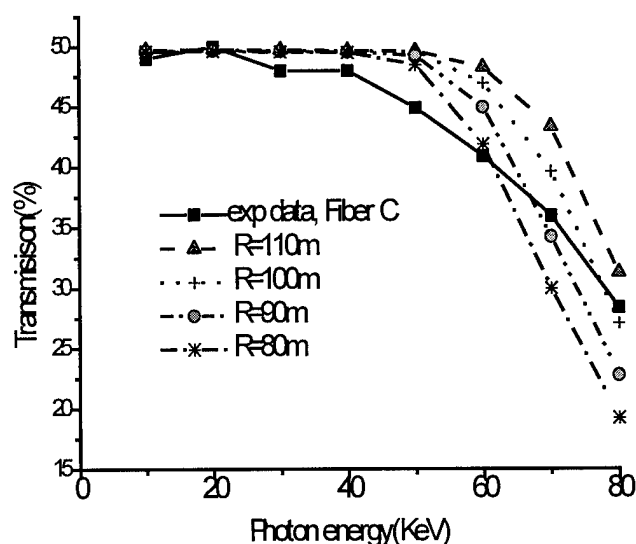


Figure 6. Transmission spectra of Fiber 3 simulated with different bending curvature alone and compared with experimental data

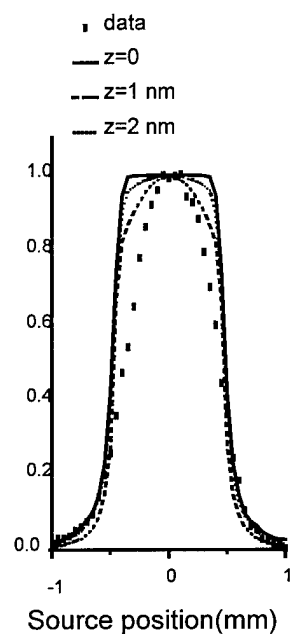


Figure 7. Source scans at 68 keV.

photons also experience fewer bounces on average.

Simulations with roughnesses as large as 1.0 and 2.0 nm still could not fit the data.

Knowing that 1.0 or 2.0 nm roughness is definitely too large at 10 keV,

we can determine that the roughness correction by itself is not

sufficient at high energy to reproduce source scan

measurements. Other effects need to be considered. These are bending and waviness.

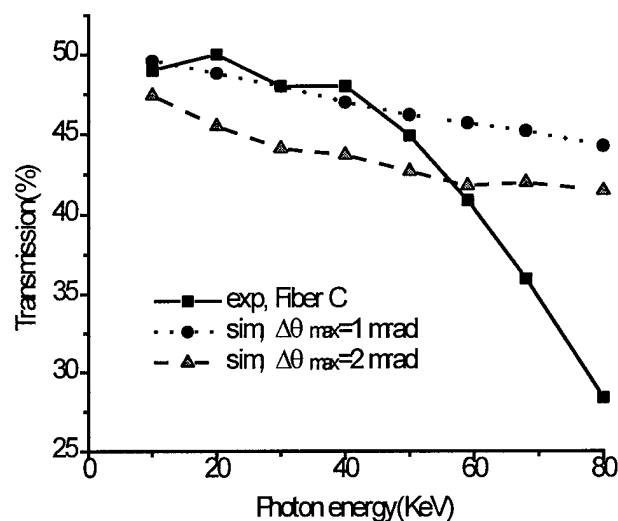


Figure 8. Simulations of transmission spectra with waviness only compared with the experimental data.

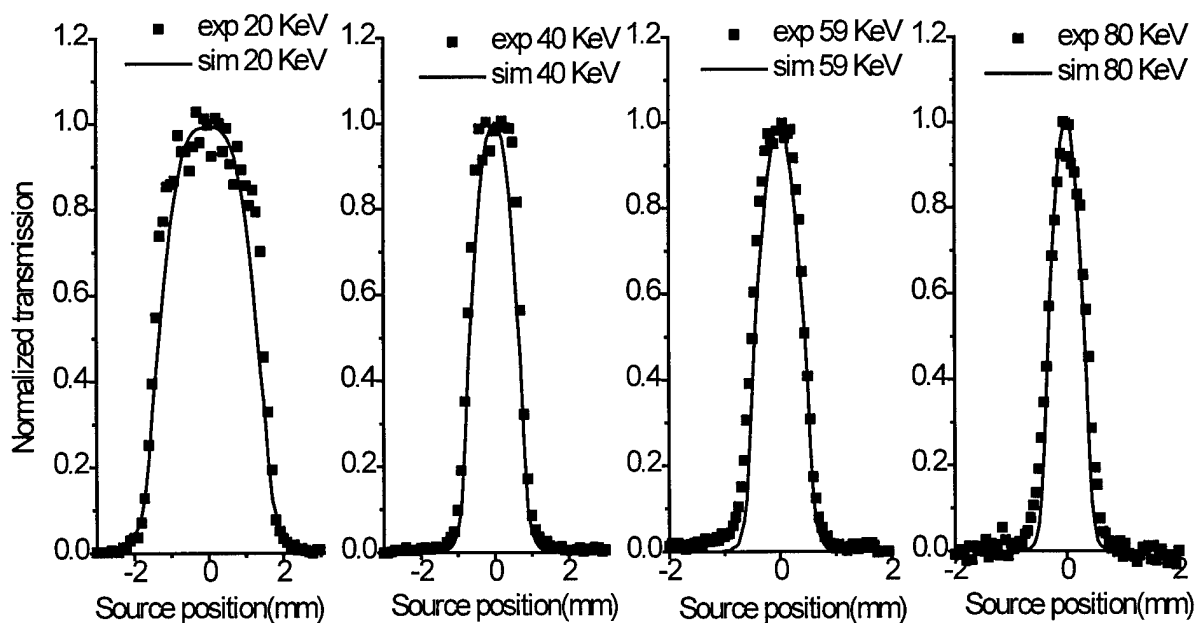


Figure 9. Simulated source scan curves compared with experimental data at four different photon energies. Parameters are: $R = 125 \text{ m}$, $\Delta\theta_{\max} = 0.35 \text{ mrad}$, roughness height = 0.5 nm.

A slight bending of the capillary can dramatically reduce the transmission of high energy photons because of the small critical angle. A comparison between experimental data and simulations with different bending is shown in Figure 6. The figure shows that the simulations with bending alone do not fit the experimental data well, which indicates that bending is not the only factor which causes the high energy transmission to drop. However, from Figure 6, we can see that the range of the bending radius must be larger than 100m to give the observed transmission at the highest energy(80KeV).

Capillary surface

oscillations with wavelengths

shorter than the capillary length and longer than the wavelength of the roughness are called waviness. The detailed shape of waviness is unknown. Its average effect can be considered as a random tilt of the glass wall, so that the grazing angle of the photon is changed by a random amount, $\delta\theta$, after every bounce. $\delta\theta$ is a random number between $-\Delta\theta_{\max}$ and $\Delta\theta_{\max}$ if $\theta \geq \Delta\theta_{\max}$. The maximum random tilt angle $\Delta\theta_{\max}$ is an adjustable parameter which depends on the waviness of the polycapillary fiber. To keep θ' positive, $\delta\theta$ is taken to be a random number between $-\theta$ and $\Delta\theta_{\max}$ when $\theta < \Delta\theta_{\max}$. Since a photon with a incident angle smaller than $\Delta\theta_{\max}$ has a larger chance to experience an

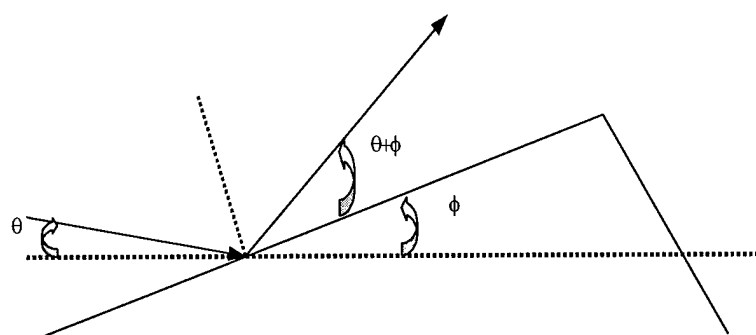


Figure 11. Scheme of an x-ray beam interacts with a random tilt surface.

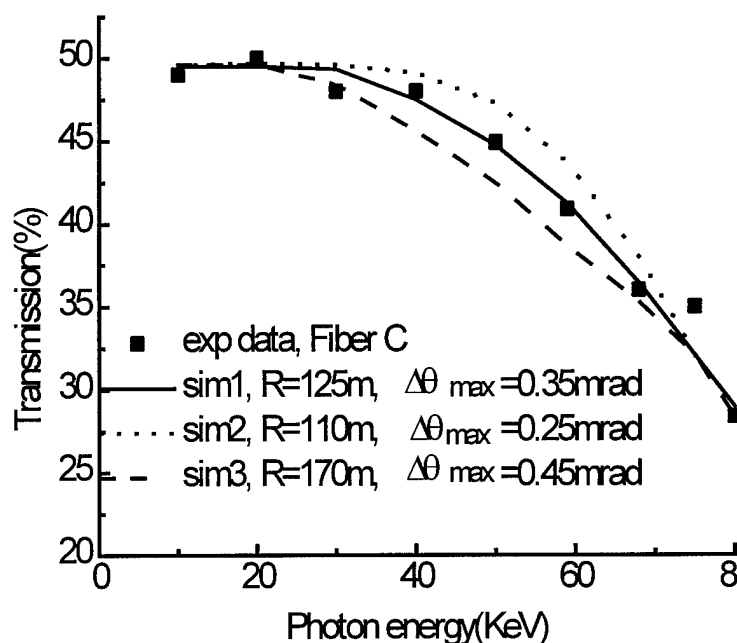


Figure 10. Simulated transmission spectra with different bending and waviness compared with the experimental data in search for the best fitting of Fiber C.

angle increase than an angle decrease, this is physically reasonable. In Figure 8, simulations with waviness corrections with $\Delta\theta_{\max}$ set at 1 mrad and 2 mrad, which is comparable to the critical angle, are compared with the experimental data. This figure shows that simulations with waviness alone do not fit the experimental data. This is because the waviness correction changes the

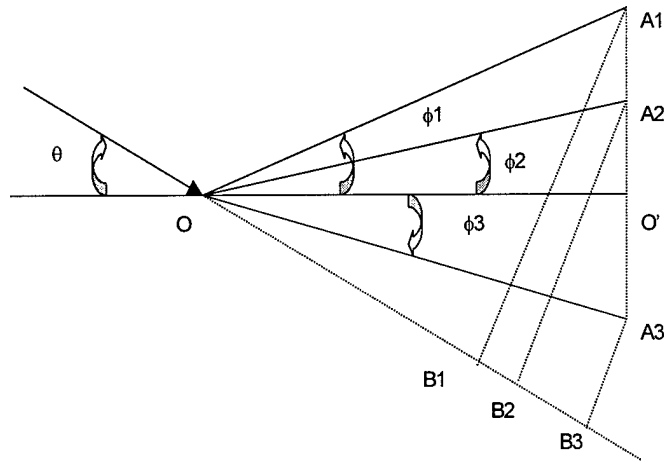


Figure 12. Three surfaces, OA_1 , OA_2 and OA_3 , with different tilt angles, ϕ_1 , ϕ_2 and ϕ_3 , respectively, from the nominal surface OO' .

reflected angle, not the profile. In fact the capillary is still considered to be straight, so those photons which have few reflections will not be significantly effected by waviness.

Finally the waviness and bending are combined by increasing the bending radius R , roughly determined in Figure 6, and adding a waviness parameter, $\Delta\theta_{\max}$. Several trials are shown in Figure 10. Sim2 has too much bending and not enough waviness; sim3 has too much waviness and not enough bending; sim1 is the best fit. Roughness is also included in those simulations. The source scan simulation with the three fixed

parameters are plotted along with the experimental data in Figure 9 for four more photon energies. They all fit quite well. This model, hereafter labeled M1, assumed a uniform distribution of tilt angles, which is not quite physical. In more recent work, discussed as Model M2, it is assumed that these tilt angles, ϕ , are normally distributed in the range $(-\pi/2, \pi/2)$ with the mean value equal to zero. For high quality optics, the standard deviation of this normal distribution, σ , is much smaller than the critical angle, θ_c . The probability distribution of tilt angles, ϕ , is

$$G(\phi) = \frac{1}{\sigma\sqrt{2\pi}} e^{-\frac{\phi^2}{2\sigma^2}}. \quad (1)$$

In this work, Model M2, consideration was taken of the fact that the surface tilt angle will affect the probability of x-ray impact on that surface. Taken to extremes, a surface region perpendicular to the beam is much more likely to intercept the beam than a surface region parallel to the beam. Figure 12 displays three surfaces, OA_1 , OA_2 and OA_3 , with different tilt angles, ϕ_1 , ϕ_2 and ϕ_3 , respectively, from the nominal surface OO' . The projections onto the nominal surface for the three surfaces are equal, $OA_1 \cdot \cos\phi_1 = OA_2 \cdot \cos\phi_2 = OA_3 \cdot \cos\phi_3 = OO'$. The probability of incidence of a parallel x-ray beam with incident angle θ (with respect to the nominal surface OO') hitting these tilted surfaces is given by their corresponding perpendicular length $A_j B_j$ (for $j = 1, 2$ or 3)

$$P_j \propto A_j B_j = OA_j \cdot \sin(\theta + \phi_j) = \frac{OO'}{\cos\phi_j} \cdot \sin(\theta + \phi_j), \quad (2)$$

We call this the tilt-corrected probability distribution. The complete description of this distribution is

$$H(\phi) = \begin{cases} \frac{F \sin(\theta + \phi)}{\cos(\phi)}, & -\theta < \phi < \frac{\pi}{2} \\ 0, & -\frac{\pi}{2} < \phi \leq -\theta \end{cases}, \quad (3)$$

where θ is the incident angle, ϕ is the tilt angle and F is a normalization constant.

Combining the normal distribution $G(\phi)$ with the tilt correction $H(\phi)$ gives $J(\phi)$ for a certain incident angle θ as follows:

$$J(\phi) = \begin{cases} K e^{\frac{-\phi^2}{2\sigma^2}} \cdot \frac{\sin(\theta + \phi)}{\cos\phi}, & -\theta < \phi < \frac{\pi}{2} \\ 0, & -\frac{\pi}{2} \leq \phi \leq -\theta \end{cases}, \quad (4)$$

where θ is the incident angle, ϕ is the tilt angle and K is a normalization constant.

Noting that

$$\frac{\sin(\theta + \phi)}{\cos\phi} = \sin\theta + \cos\theta \cdot \tan\phi \quad (5)$$

and that both the incident angle, θ , and the tilt angle, ϕ , are very much less than 40 mrad, we use the approximation

$$P(\phi) = \begin{cases} C e^{\frac{-\phi^2}{2\sigma^2}} * (\theta + \phi), & -\theta < \phi < \frac{\pi}{2} \\ 0, & -\frac{\pi}{2} \leq \phi \leq -\theta \end{cases}, \quad (6)$$

where the normalization constant, C , is

$$C \approx \frac{1}{\sqrt{2\pi\theta\sigma + 2\sigma^2}}, \quad (7)$$

to speed the calculation. $P(\phi)$ is called the tilt-corrected normal distribution. In model M2, σ is the variable that describes the amount of waviness. An example of $J(\phi)$ and $P(\phi)$ is shown in *Figure 13*. The result of the waviness calculation is shown in *Figure 14*. The model M2 shows a much larger drop at high photon energies for lower values of the waviness than does model M1.

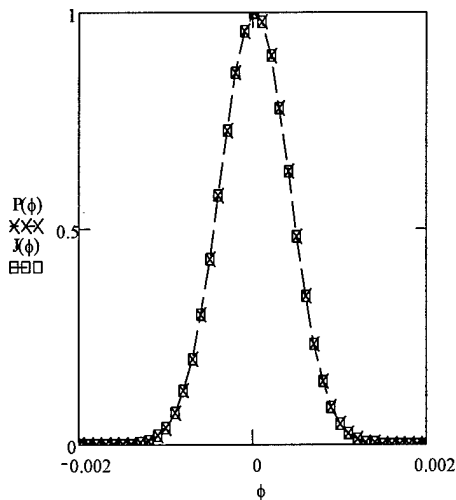


Figure 13. $P(\phi)$ and $J(\phi)$ versus tilt angle ϕ when incident angle $\theta = 0.009\text{rad}$, standard deviation $\sigma = 0.0004\text{rad}$. ϕ is in rad.

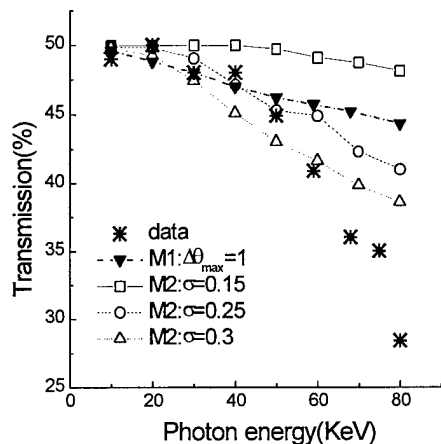


Figure 14. Simulations of transmission spectra for fiber C with only waviness compared with the experimental data. This figure shows the effects of waviness. It also shows simulations using waviness alone do not fit the data. The simulations do not include roughness or bending.

A comparison of the simulation with bending and waviness to the experimental data is shown in Figure 15.

Using a similar technique, the simulation was compared to the fibers listed in Table 1, using the parameters listed in Table 2. The results are plotted in Figure 16 and Figure 17. In Figure 16, the transmission for fiber A shows a rapid drop for energies above 30 keV. Although fiber D has lower fractional open area than fiber A, its transmission exceeds that of fiber A at energies above 30 keV. This is because fiber A is thin (0.5 mm in outer diameter) and flexible, therefore difficult to keep straight in the measurement apparatus. Model M2, which can vary only bending and waviness, requires a much sharper bend for fiber A than for fiber D. This bending is more significant at high energies, where the critical angles are smaller.

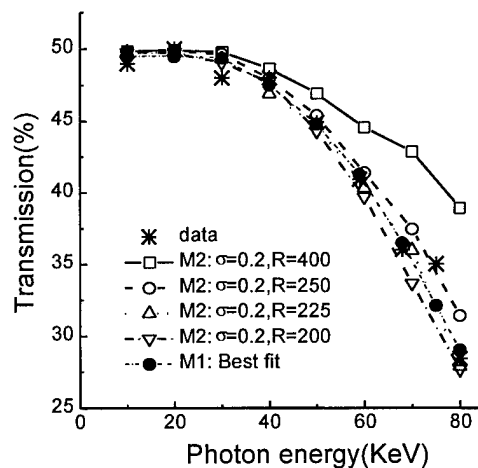


Figure 15. Simulated transmission spectra using model M2 with fixed waviness ($\sigma = 0.2\text{ mrad}$) and different bending (bisection method), compared with the experimental data. The simulation curves shown are just a few representative cases in the bisection process. For M2, the best-fit parameters are $\sigma = 0.2\text{ mrad}$ and $R = 225\text{ m}$; for M1, they are $z = 0.5\text{ nm}$, $s = 6\text{ }\mu\text{m}$, $\Delta\theta_{\text{max}} = 0.35\text{ mrad}$ and $R = 125\text{ m}$.

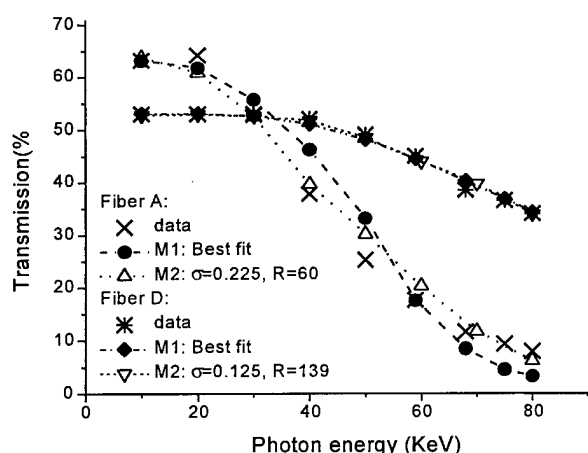


Figure 16. Simulations of transmission spectra of fiber A and fiber D with their best-fit parameters compared with the experimental data. All parameters related to this figure are listed in Table 1.

However, if the channel size is too small, as in fiber E, it also results in more reflections being needed for a photon to traverse the fiber and may have introduced other defects such as blocked channels. This is why the transmission is only 40% for the energies below 40 keV although the open area is around 55%.

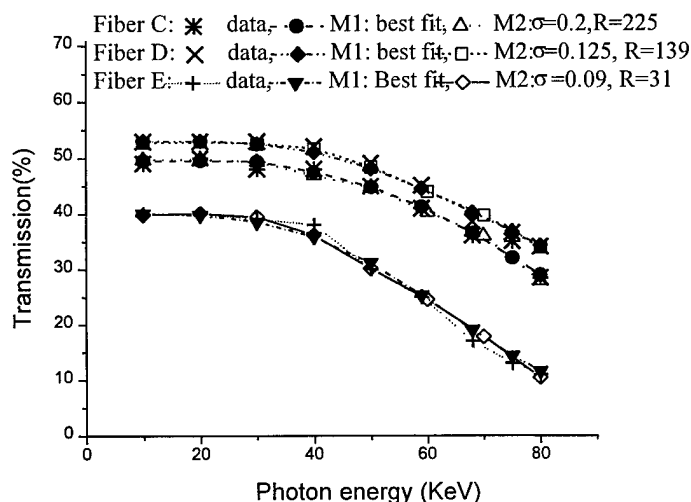


Figure 17. Simulations of transmission spectra of fiber C, fiber D and fiber E with their best-fit parameters compared with the experimental data. All parameters related to this figure are listed in Table 2.

Transmission curves for fiber C and D are similar in shape and are nearly flat up to 60 keV, as shown in Figure 17. However, the smaller channel size for fiber D results in the simulation being less sensitive to bending. Therefore a larger bending curvature (smaller radius) is required for fiber D. The waviness correction for fiber D must therefore be smaller to keep the transmission about the same as for fiber C.

Fiber E is the thinnest fiber. Table 2 shows that it has the largest bending correction because of its flexibility. Its transmission curve is flat up to 40 keV. This is due to its very small channel size, as discussed in the comparison of fiber C and fiber D.

The new model yields as high a quality fit with two fewer fitting parameters than used in model M1 in Figure 4. The high transmission and the simulation results show that the quality of the capillary fibers is quite good. The bending radius is above 130 meters for type 3 and type 4 capillaries. It is hopeful that we can further improve the high-energy transmission performance of polycapillary fibers by decreasing to an optimum channel size, and making them more rigid.

Fiber Description						Model M1				Model M2	
Fiber #	Type	Outer Diameter (mm)	Channel Size (μm)	Area	Length (mm)	z nm	s μm	R m	$\Delta\theta_{\text{max}}$ mrad	R m	σ Mrad
A	1	0.5	12	65%	105	0.7	6	105	0.4	60	0.225
C	3	0.75	22	50%	136	0.5	6	125	0.35	225	0.2
D	4	4	12	55%	130	0.8	6	110	0.285	139	0.125
E	5	0.3	4-5	55%	105	0.7	6	28	0.2	31	0.09
F	4	4	12	55%	130	0.8	6	90	0.45	90	0.18

Table 2 Parameters for best-fit simulations. R is the bending radius. For M1, $\Delta\theta_{\text{max}}$ is the amount of waviness, z is the roughness height and s is the roughness correlation length. For M2, σ is the standard deviation of the waviness.

Fiber B in Figure 4 has poor transmission; it is a lead glass fiber, with high surface roughness and waviness. More recently, higher quality lead glass fibers have been produced. The transmission as a function of photon energy for these fibers is shown in Figure 18. These leaded fibers have higher absorption of high angle photons than the lower density borosilicate glass fibers, and therefore would provide even better scatter rejection, as is described in section 6.3.3.

Transmission was also measured of deliberately curved fibers, which can be used to deflect x-ray beams over larger angles. The results are shown in Figure 19.

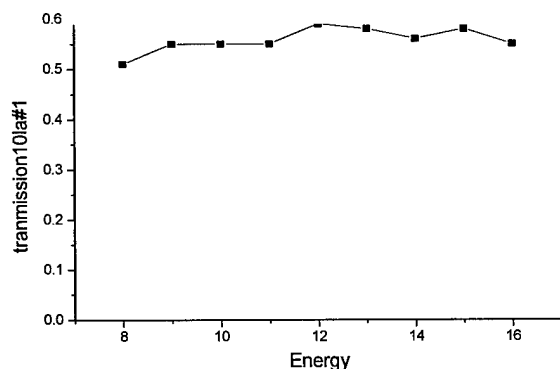


Figure 18. Recently manufactured lead glass fibers.

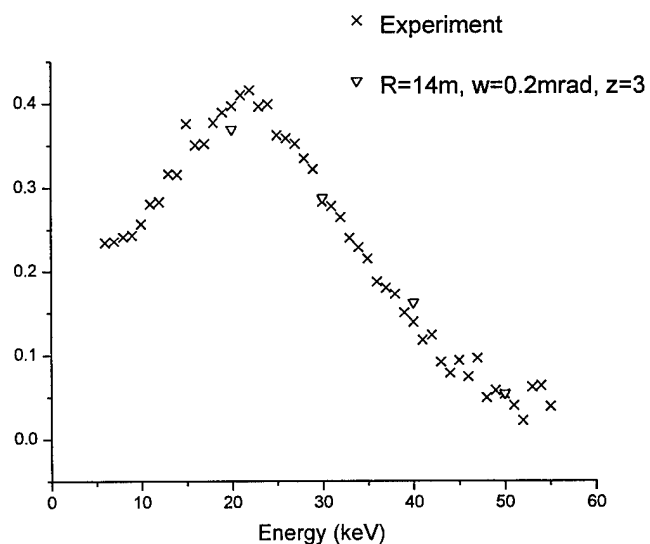


Figure 19. Transmission efficiency of 350 μm OD polycapillary fiber with 6 μm channel diameter. The fiber length is 25 cm. Simulated values are shown for 20, 30, 40, 50 keV x rays. The parameters are curvature, R ; waviness, w ; and roughness, z .

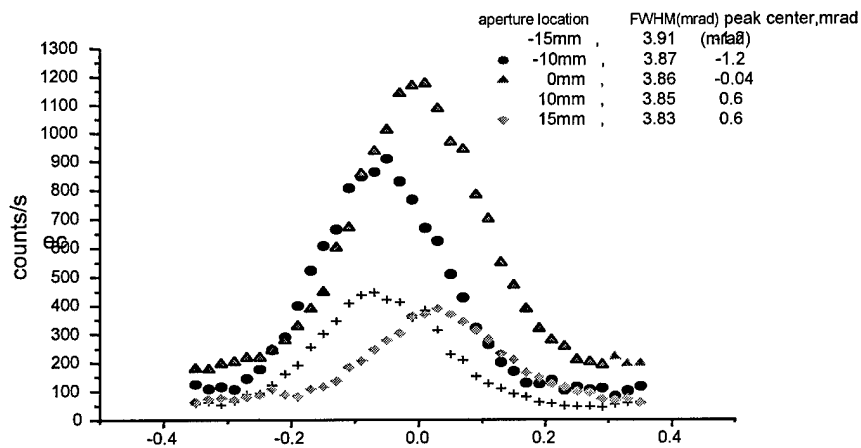


Figure 20. Measured local divergence of the output of multi-fiber I at 8 keV.

6.2. SIMULATION OF MULTIFIBER OPTICS

Measurements of the exit divergence of the collimating optic have been performed at 8 keV and at 20 keV. Exit divergence is important if a capillary optic is to be used as a collector fore slit before the patient. In this case, the spatial resolution will depend on the angular spread of x-rays at the exit end of the polycapillary fibers.

Large angular divergence is equivalent to a large focal spot size in a conventional system.

The divergence can also be used to assess fiber alignment in the lens. The beam exiting the optic is characterized by a divergence that arises from two effects. The first is the local divergence of the x-rays emerging from each channel, usually between θ_c , the critical angle for total reflection and $2\theta_c$. There is also fiber misalignment, the deviation of the individual channel axis direction from the optic axis direction. Local divergence depends upon the surface roughness,¹³ waviness, and bending of fibers through the optic. Figure 20 shows the measured local divergence of the output of the collimating lens at 8 keV with the aperture at -15 cm, -10 cm, 0 cm, 10 cm and 15 cm off the axis of the lens. The FWHM of each divergence curve is in the range of 3.8 mrad to 3.9 mrad, which is very close to the critical angle of about 4 mrad at 8 keV. The peak centers of these five local divergence curves are systematically shifted. This shift could be caused by the output ends of the fibers inside the lens being slightly convergent

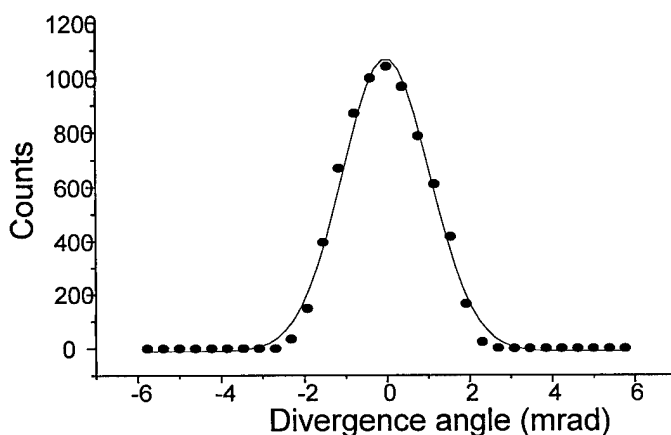


Figure 21. An ideal whole lens simulation at 8 keV gives a divergence FWHM of 2.5 mrad.

rather than parallel. The widths of the measured local divergence curves shown in Figure 20 are larger than that predicted by an ideal lens divergence simulation, shown in Figure 21.

The divergence of the modeled ideal lens is low because the nearly straight central fibers, if ideal, would not increase the divergence above the entrance divergence due to the source spot size. Figure 23 shows the simulated divergence profile of x-

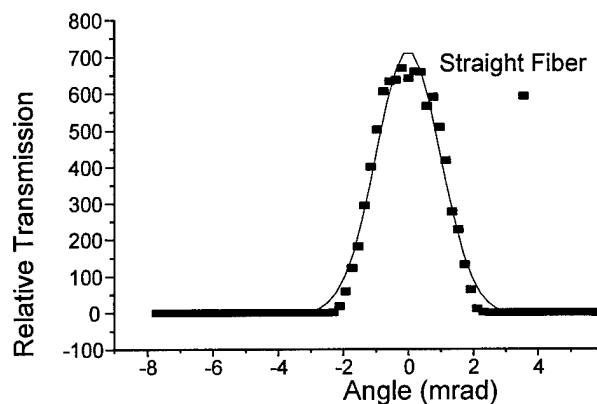


Figure 23. For an ideal fiber (with no surface defects), the divergence simulation yields a FWHM of 2.36 mrad at 8 keV.

The simulations in Figure 21 and Figure 23 did not include the effects of profile defects and waviness. Waviness will increase the angle of reflection for x-ray photons for most bounces inside the channel. Consequently the divergence from the lens increases. Figure 22 shows a simulated transmission of a straight fiber as a function of exiting angle, using a waviness of $\omega = 0.15$ mrad. The width of the simulated divergence curve for this straight fiber is about 4.0 mrad, which is close to the local divergence at the center of the lens shown in figure 16. Waviness of the channels changes the divergence of the x rays exiting from the center of the lens from about 2.4 mrad to 4.0 mrad.

6.3. MAGNIFYING LINEAR MONOLITHIC ANTISCATTER OPTICS

6.3.1. TRANSMISSION

Linear monolithic optics taper as a single glass unit from input to output as shown in Figure 28. These optics are relatively difficult to manufacture. Many early prototypes have poor transmission, as shown in Figure 24. To help understand the defect problem an extensive simulation and measurement study was performed on several of the prototypes.

Transmission of a monolithic taper is plotted versus source lens distance in Figure 25 along with the simulation values.

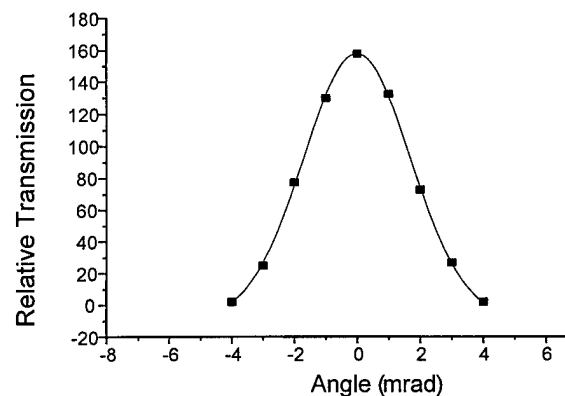


Figure 22. A simulation with a waviness of 0.15 mrad increases the divergence value from 2.4 mrad for an ideal straight fiber to 4.0 mrad.

rays exiting from an ideal straight fiber, which has a FWHM of 2.36 mrad.

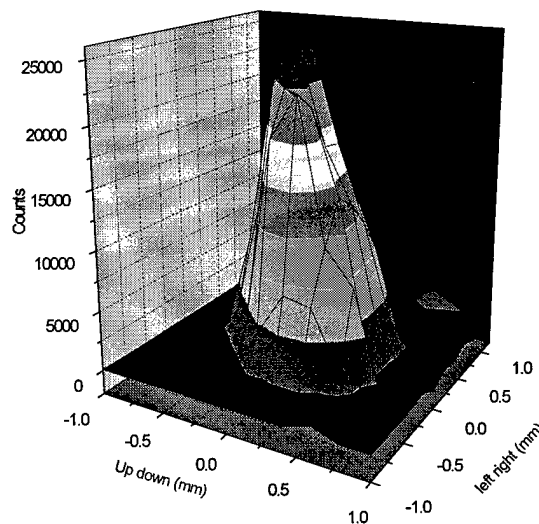


Figure 24. 2-D source scan of early prototype optic (input diameter = 2 mm, output diameter = 3 mm, transmission = 5 % at 20 keV, focal distance 22 cm) This lens transmits poorly because only the central capillary channels transmit while the outer capillaries do not transmit at all. Only about 33 % of the optic cross section transmits at 5 % or greater.

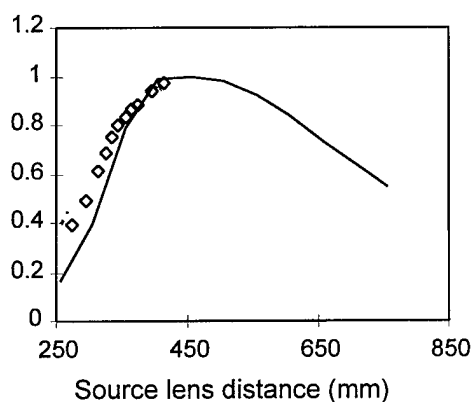


Figure 25. Transmission of tapered lens. Solid line is simulation.

The maximum point for transmission is around 450 mm. The second method can be affected by the source instability.

Transmission was measured in a wide energy range for the whole lens as well as the central part of the lens. The transmission spectrum for the whole lens is plotted in Figure 26. The

figure shows that the transmission drops quickly for photons with energy higher than 20 keV, but the transmission under 20 keV is almost flat. The low transmission in the high energy range can be explained by the non-linearity of the lens. The outermost channels are more bent than the central channels, so they have low or zero transmission at the higher photon energies. This is confirmed by the higher transmission measurement at the central part of the lens, shown in Figure 27 and the transmission uniformity

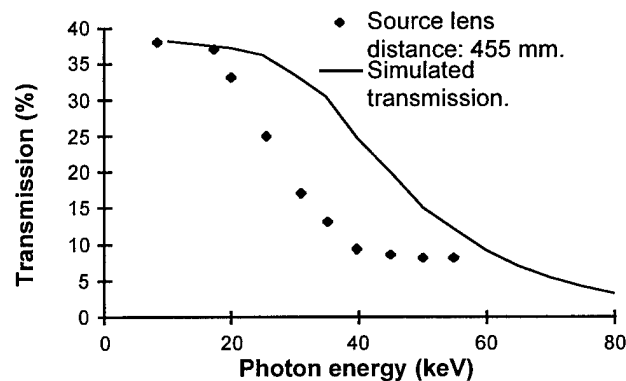


Figure 26. Transmission of whole tapered lens.

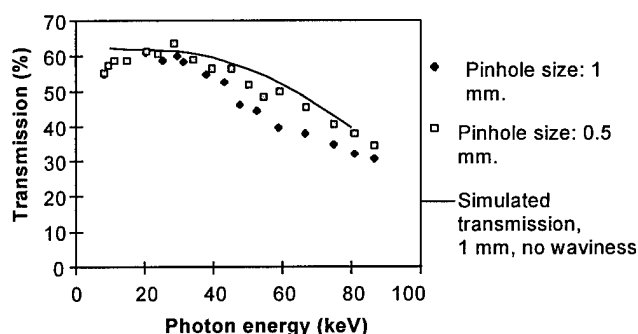


Figure 27. Transmission of the central part of the tapered optic.

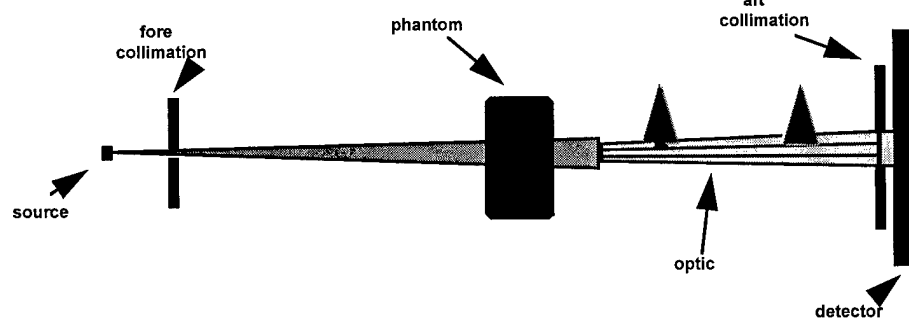


Figure 28. Small optic scanning geometry for contrast and imaging measurements.

measurement at different energies, shown in Figure 29. Transmission uniformity of the lens was measured by putting a 200 μm pinhole in front of the lens and performing a two dimensional scan. At 8 keV, the whole lens transmits,

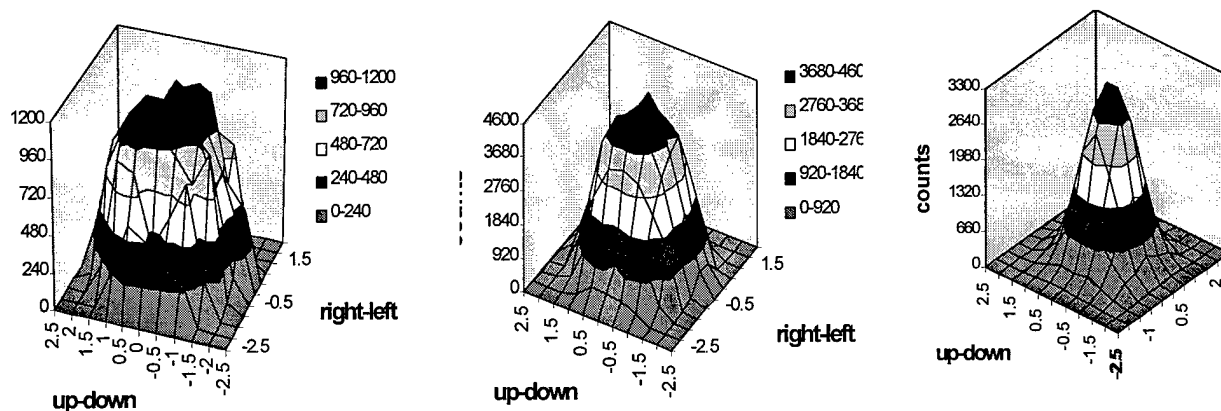


Figure 29. Two dimensional scans of the output of the tapered optic.

although we can see the transmission is not completely flat due to the non-linearity and the defects of the lens, such as blocked channels. At 25 keV, transmission of the whole lens drops to 25%. Most of the lens is still transmitting at 25 keV, but the outer channels have lower transmission than the central part. At 35 keV, the lens has a narrower transmitting region. The measurements show that the lens has undesirable nonlinearity.

6.3.2. SIMULATIONS

Modeling defects, including waviness, bending, and blockages, require sophisticated simulations. The simulations plotted in Figure 25 and Figure 26 used the same roughness and waviness correction as that used for fiber D in Figure 4. A linear tapered lens is ideal for mammography, because, as shown above, any curvature can cause transmission reductions. However, the lenses currently available have nonlinear profiles. The profile is not circular, but to simplify the simulation, we assume that the profile is circular. A uniform bending will provide the best transmission performance for

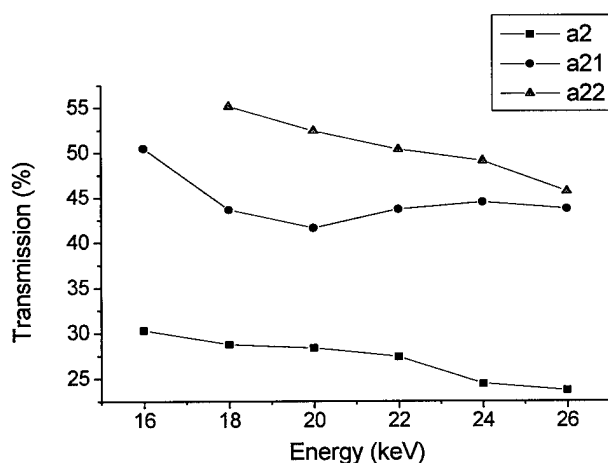


Figure 30. Transmission of final half of A (A2), and its two constituent pieces, the first 5.5 cm, A21 and the final 5.5 cm, A22. A21 contains a defect.

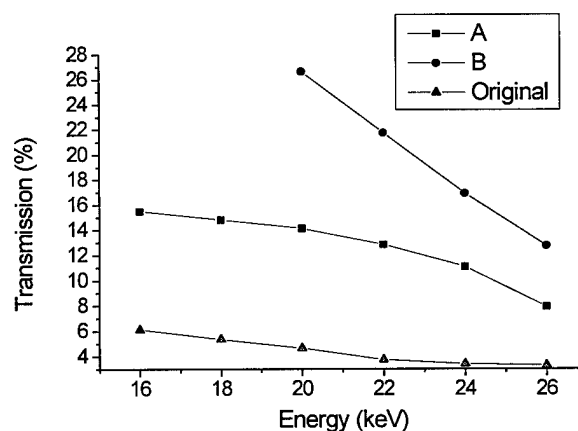


Figure 31. Transmission of original optic compared to two pieces. B is the first 10 cm (closest to the source), A is the final 22 cm.

a given bending angle, so the simulation will overestimate the lens performance. A further simplification assumes the lens has a fixed channel size, although the channels actually taper with the lens.

The geometry for uniformly bent nonlinear lenses is shown in Figure 32. The simulation method for a uniformly bent lens is an extension of the simulation for uniformly bent polycapillary fibers. The simulation is done by sampling channels in the input cross section of the lens

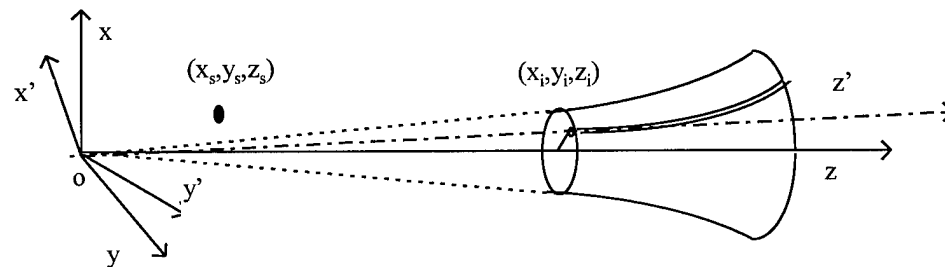


Figure 32. Geometry for Lens simulation.

with an even step size. In the simulation for a bent fiber it is assumed that the capillary bends in -y direction, and z direction is along the input axis of the fiber. In order to reuse the old simulation code, the coordinate of the simulation x-y-z is rotated to x'-y'-z', where z' is the direction of channel axis at the input end and -y' is the channel bending direction. Assuming the source position and the capillary position at input end is (x_s', y_s', z_s') and $(0, 0, z_i')$ respectively, then the source capillary distance is $z_i' - z_s'$. The origin of the coordinate is selected to be the focus point of the lens.

Another parameter needed by the simulation is the bending curvature of the selected channel. This value varies with the position of the channel. The calculation of the bending curvature is demonstrated in Figure 33.

First it is assumed that the channels are evenly distributed on both input and output cross section. Let input and output diameter of the lens be r_i and r_o , and focal distance \overline{OA} be f , and the lens length \overline{AC} be L , then

$$\overline{AB} = \sqrt{x_i^2 + y_i^2}, \quad \overline{CE} = \overline{AB} * r_o / r_i$$

For a small bending angle, $f / (f + L) = \overline{AB} / \overline{CD}$, $d = \overline{CE} - \overline{CD}$
 $\alpha \approx L / R = d / (L / 2)$

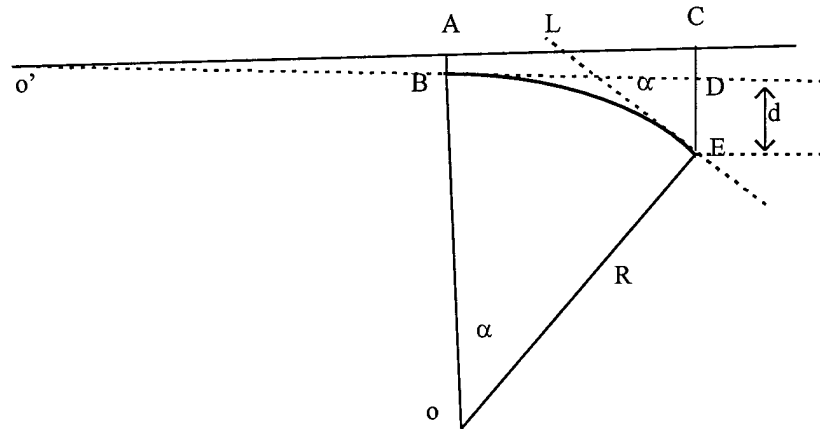


Figure 33. Curvature estimation for lens simulation.

where R is the bending radius, d is the distance between point D and E as shown in Figure 33, and α is the bending angle. Thus

$$R = L^2 / 2d \quad (8)$$

The simulated results in Figure 26 and Figure 27 show higher transmission than the experimental results. This indicates that the lens has more reduction in transmission due to the bending. This is expected, because the lens does not have a uniform bending.

6.3.3. POTENTIAL FOR LEAD GLASS

Transmission from early fibers was poor in the whole energy range. Recent fibers are more promising. Transmission for an early 95 mm long and a more recent 125 mm long lead glass polycapillary fiber is shown in Figure 34. The transmission drop at lower energies may be caused by partially blocked channels. Transmission can also be improved by using a short optic. Almost total scatter rejection is expected for a lead glass optic longer than 30 mm.

6.3.3.1. CALCULATION OF CONTRAST IMPROVEMENT AND RELATIVE SNR

Lenses with large diameters are not currently available. Their potential behavior can be predicted by scaling up existing measurements to a large area lens, as shown in Figure 35. The value of h is the length of the optic. For a point P on the film, scattered radiation could come from any direction in the solid angle Ω_{patient} , which is the solid angle subtended by the patient. The transmission for scattered x rays can be calculated from the mass absorption coefficients. The calculated scatter transmission depends on the length of the photon path through the optic. Making a very conservative estimation, we can fix this length to the length of the optic. There is also a small part of the scattered x rays that have almost the same direction as those primary x rays. This part of the scattered x rays with an incident angle less than critical angle could still pass through the channel. So the total scatter transmission of the lens is

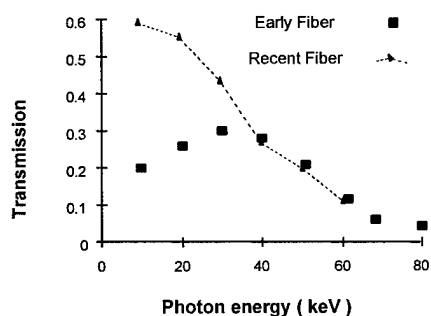


Figure 34. Transmission as a function of photon energy for a lead glass capillary. The fibers are 105-120 mm in length.

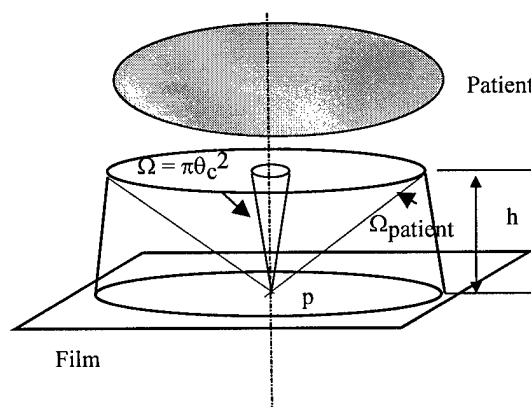


Figure 35. An ideal large area lens.

Table III. Transmissions for three lenses. The results for the ideal borosilicate lens are measured results for the center part of the prototype lens. The results for lead glass lens are simulated with 120 kVp spectrum and a W target.

Lens #	Lens type	Length (mm)	Photon Energy	Primary transmission $T_{p-optic}$	Scatter transmission $T_{s-optic}$
1	Ideal borosilicate Lens. Scaled up from the center part of the prototype lens	166	20 KeV	0.6	0.0
			45 KeV	0.55	0.002
			60 KeV	0.55	0.005
			70 KeV	0.45	0.03
2	Actual Borosilicate prototype lens	166	20 KeV	0.33	0.0
3	Lead glass	30	69 KeV	0.63	0.0076

$$T_{s-optic} = \frac{N_{s-optic}}{N_s} = T_s + \frac{T_p \cdot \pi \theta_c^2}{\Omega_{patient}}, \quad (9)$$

where $N_{s-optic}$ is the number of scattered x rays with the optic, N_s is the number of scattered x rays without the optic, T_s is the transmission for large angle scattered x rays, T_p is the transmission for primary x rays, $\Omega_{patient}$ is the angle subtended by the patient, θ_c is the critical angle for transmission in the channels. Because the critical angle is on the order of 10^{-3} radians, the second term is very small, and can be ignored. So scatter transmission of the lens can be estimated to be equal to large angle scatter transmission, T_s , which can be calculated from equation **Error! Reference source not found.**, and nearly scatter free lenses can be obtained by using a suitable length optic. In the above equation, we assumed that the angular distribution of the scattered x rays is isotropic. If the scatter distribution is not isotropic, the second term in equation (9) can be larger than expected, but will still be very small, and this assumption will not significantly effect the result. In equation (9), T_s , T_p and θ_c are all energy dependent. In the case where x rays with a wide x-ray spectrum are used, T_s and T_p should be replaced by the average large angle transmission and primary transmission. To avoid underestimating scatter transmission, θ_c can be set to be the critical angle for the lowest energy in the spectrum.

The scatter and primary transmission of the optic determine the performance of the capillary lens. For example, if the scatter fraction before the capillary lens is F , then the scatter fraction after the lens, F_{optic} , is

$$F_{\text{optic}} = \frac{F \cdot T_{s\text{-optic}}}{F \cdot T_{s\text{-optic}} + (1 - F) \cdot T_{p\text{-optic}}} = \frac{KF}{1 - F(1 - K)}, \quad (10)$$

where $T_{p\text{-optic}}$ is the primary transmission of the lens and K is the ratio

$$K = \frac{T_{s\text{-optic}}}{T_{p\text{-optic}}}. \quad (11)$$

The contrast enhancement achieved by using the optics is

$$\frac{C_{\text{optic}}}{C_{\text{no-optic}}} = \frac{1 - F_{\text{optic}}}{1 - F} = \frac{1}{FK + (1 - F)}. \quad (12)$$

The contrast enhancement alone is not the only relevant quality factor. The signal to noise ratio (SNR) is another important quality factor. According to the Rose model,

$$k^2 = C^2 \Phi A, \quad (13)$$

where k is the SNR, C is the contrast, Φ is the photon flux, and A is the area of the target. In order to compare the SNR for different scatter rejection devices, relative SNR was used. Relative SNR is the SNR normalized by the SNR without any scatter rejection device,

$$k_r^2 = \frac{k^2}{k_0^2} = \frac{C^2}{C_0^2} (FT_s + (1 - F)T_p), \quad (14)$$

where k_r is the relative SNR. C and C_0 are the contrast with and without out the scatter rejection device, respectively. T_s is the scatter transmission and T_p is the primary transmission of the device.

6.3.3.2. PERFORMANCE OF THREE HYPOTHETICAL LENSES

Performance estimates of three hypothetical lenses are given in Table III. The ideal borosilicate lens is scaled up from the center part of the measured lens. Simulated transmission was used for the lead glass lens. The performance of the three lenses was compared with the performance of the conventional grids described in Table IV. The primary and scattered transmissions of the different grids in Table IV were measured at 69 keV, which is the average energy of the 120 kVp tungsten spectrum, and with

scatter fraction of 85%, by C. E. Dick and J. W. Motz¹⁴. It is assumed that the scatter and primary transmission are the same under different scatter fraction. This assumption is correct if the angular distribution of the scattered x rays does not change. The performance of the grids is assumed to be energy independent. They might perform better at lower photon energies if the scatter transmission is due to the lead plates which are not thick enough to absorb the incident x

Table IV. Performance for several commercial grids, measured at a scatter fraction of 85%.¹⁴

Grid ratio	Primary transmission at 69 keV	Scatter transmission at 69 keV
6	0.73	0.27
8	0.64	0.13
12	0.61	0.071

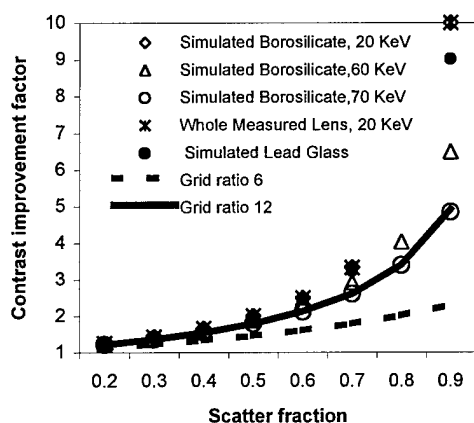


Figure 36. Contrast improvement vs. scatter fraction for the three lenses. The results were compared with the performance of two commercial grids.

measured lens. This lens has good contrast improvement because of its total scatter rejection. However its relative SNR is lower than that of the grids when the scatter fraction is less than 80% because of its low primary transmission. The primary transmission of this lens is only 33% and the primary transmissions for all the three commercial grids are better than 60%. So with this lens more exposure will be necessary to the patient. Overall primary transmission has to be improved for practical use. Lens#1 is scaled up from the center part of the measured lens. From the

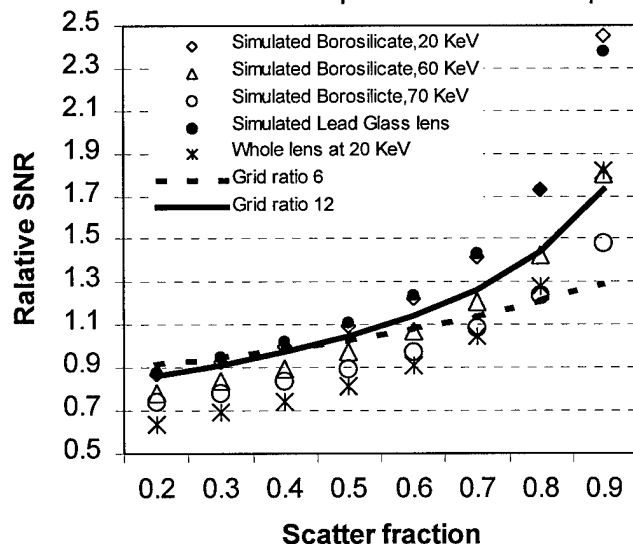


Figure 37 Relative Signal to Noise(SNR) vs. scatter fraction for three hypothetical lenses. The results were compared with the performance of three commercial grids.

rays. However, it was assumed the dominant mechanism for scatter transmission was x rays passing through the interstitial material. The contrast enhancement and relative SNR were calculated under different scatter fractions and plotted in Figure 36 and Figure 37.

For most medical x-ray imaging applications, the effective energy ranges from 20 to 70 keV.

Mammography has an effective energy of 20 keV. The results in Figure 36 show that contrast improvement of all the three hypothetical lenses are better than or as good as that of the three grids. Lens #2 is scaled up from the whole

calculations, summarized in Figure 36 and Figure 37, its performance is significantly better than those of the commercial grids for effective energies of 20-45 keV. This lens will not only improve the contrast in the imaging but also reduce the exposure time to the patient. So it is ideal for mammography.

Assuming that the lead glass capillaries have the same quality as that of borosilicate fibers, we can estimate the performance of a lead glass lens. Simulations of transmission spectra were performed for a source to lens distance of 1.5 m, and the source operated at 120 kVp with a 0.5 mm spot size. For a perfect lens, each channel in the lens is tapered. With a tapered channel, fewer average reflections will be needed for the photons to pass. So

theoretically, transmission with a perfect lens is larger than for a straight capillary if they have the same quality. The transmission is quite sensitive to the capillary length. Therefore, as long as the lens has low enough scatter transmission, the length of the lens should be kept as short as possible. The performance estimation results of the lead glass lens in Figure 37 are based on the simulated transmission with length of 30 mm. The scatter transmission of this lens is less than 1%. Primary transmission as high as that of grid is also obtained with simulation.

Compared to the grid performance, this lens has higher contrast enhancement and relative SNR. So this lens will not only improve the contrast of the image, but also reduce the radiation dose to the patient.

6.3.4. MTF CALCULATION

Modulation Transfer Function (MTF) is the most fundamental measurement of spatial resolution used in radiology. The standard technique is to image a slit, determine the line spread function (LSF), and compute the Fourier transform. The MTF measured for the mammography system with capillary optics, compared to that without the capillary optics, will give the resolution improvement and also can be used to diagnose artifacts.

The structure of the capillary bundles was obvious. In this case, the LSF could not be obtained by imaging a slit without background elimination. The background deducted slit image is the slit image divided by the image with capillary only. However, this involves image registration. The information for background that can be used for image registration is too little in the slit image. An alternative method is calculating the LSF as the derivation of the edge spread function (ESF). The edge image left enough background for registration so that it could be a feasible method in our case.

A registration algorithm (FMI-SPOMF) proposed by Chen, et al.¹⁵ was used in this work. This is a method to match a two-dimensional image to a translated, rotated and scaled image. The approach consists two steps: the calculation of a Fourier-Mellin Invariant (FMI) descriptor

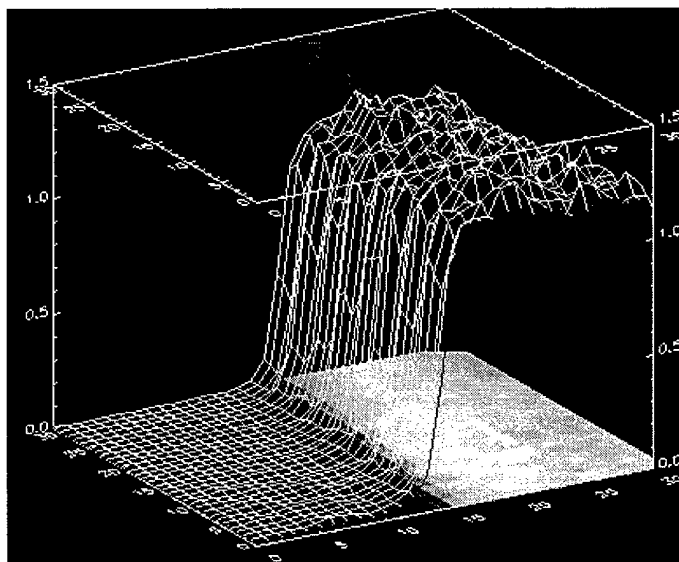


Figure 39 Three-dimensional edge image after background subtraction.

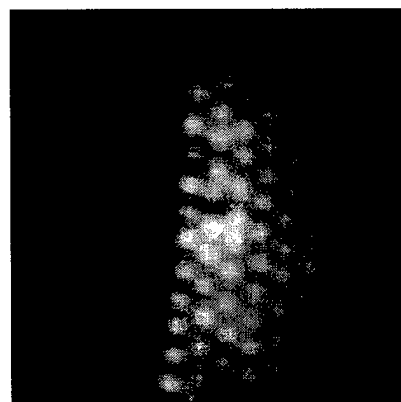


Figure 38. Magnified image of a lead edge. Real image size: 5(mm) X 5(mm).

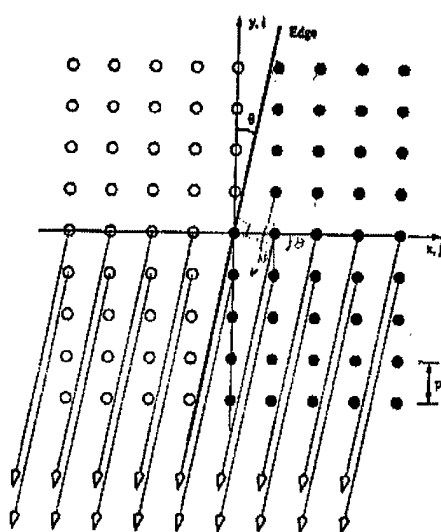


Figure 41. Reprojection of a two-dimensional edge image into a finely sampled ESF.

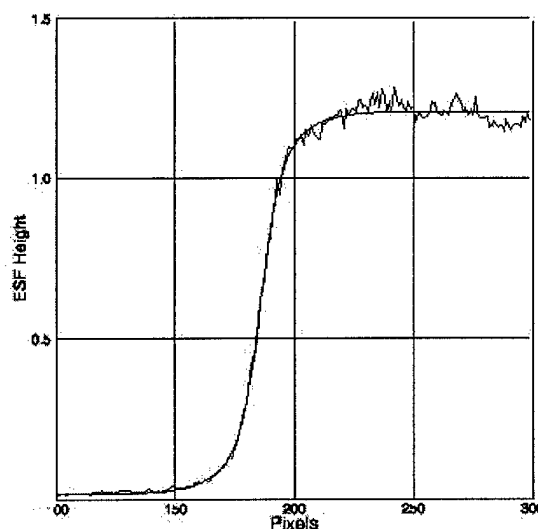


Figure 40 Edge spread function and its fitting curve.

for each image to be matched, and then matching of the FMI descriptors. FMI descriptors are translation invariant. The matching of the FMI descriptors is to find out the rotation and scaling, and achieved using a symmetric phase-only matched filtering (SPOMF). In our case, there is no change in scaling, but rotation is probably involved. When the rotation was found, image translation is found by SPOMF method.

Images were taken with and without edge as shown in Figure 38. The edge was made of a lead plate. The size of each image is fifty by fifty in pixels. They were taken in an experimental digital mammography system with a computed radiography digital phosphor plate. The digital CR plate has limited resolution, 5 lp/mm, and is usually considered to be not good enough for clinical mammography. But the effective resolution of the system could be improved by the magnification of the capillary optics. The magnification of the capillary lens used in the system is 1.86, so that the effective resolution should be improved by a factor of 1.86.

The registration algorithm was implemented in IDL. With the FMI-SPOMF registration algorithm, no rotation was found. The translation was then found by SPOMF algorithm. The difference between the usual correlation method and SPOMF method is that it only uses the phase information. The phase-only correlation function has sharper peak than normal correlation function. Sub-pixel resolution could be achieved theoretically. However it was found that the resolution is not good enough in our case. This may be caused by the relatively small image size. The background-subtracted result was further optimized by manual shifts in sub-pixel range. The result after manual optimization was shown in Figure 39. The periodic background is totally gone. A cubic spline interpolation method was used for the best result while shifting the background image relative to the edge image.

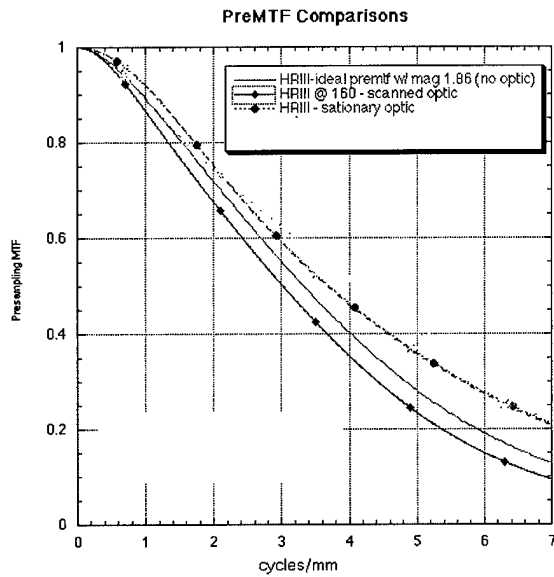


Figure 42 Calculated MTF compared with the MTFs with scan optics, and without optics.

The presampling MTF includes unsharpness of the detector and the sampling aperture. In order to eliminate the aliasing, a finely sampled ESF is obtained with a slightly angulated edge in a single exposure as illustrated in Figure 41.^{16,17} The angle in our edge image in Figure 39 was calculated to be around 6°. The resultant ESF is plotted in Figure 40. A direct calculation of MTF is to take the derivation of the ESF and result a LSF, then take Fourier transform. As it can be seen, the ESF in our case is not smooth enough for a direct calculation. An alternative technique is to use an ESF fitting procedure.¹⁸ In the fitting method, the ESF is represented with a term (1-exp) and an error function (erf) as in equation (15). MTF is calculated by equation (16), where a, b, c and d are fitting parameters from equation (15). The fitting curve is plotted in Figure 40 as the solid line.

$$ESF(x) = a\{1 - \exp(-b |x - x_0|)\} + c \cdot \text{erf}(d^{1/2} |x - x_0|) \quad (15)$$

$$MTF(f) = \frac{c \cdot \exp(-\pi^2 f^2 / d) + a(1 + 4\pi^2 f^2 / b^2)^{-1}}{(c + a)} \quad (16)$$

The calculated MTF was compared with that from scanned optics in Figure 42. The MTF from scanned optics was calculated from a slit image. Optic structure was smeared out with scanning, so no background deduction is necessary. An ideal MTF was also plotted in Figure 42. An ideal MTF is the one when we assume the lens

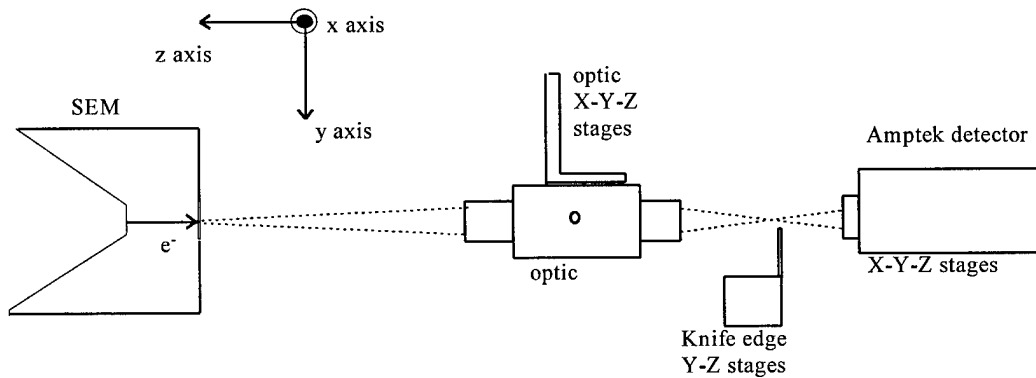


Figure 43. Schematic of the experimental setup for optic characterization.

introduces only the 1.86 factor magnification and no image degradation. It is measured with a slit image without optics, and its result was multiplied by the magnification of the capillary lens. The measured MTF with lens should no better than the ideal MTF. However, for some reason, the MTF for stationary lens is better than the ideal MTF. It is possible that the background elimination process failed the MTF measurement. Another possibility is that the magnification of the lens is different from 1.86, since the magnification was measured separately at a different time.

7. Key Research Accomplishments

- Development of extensive modeling capability for polycapillary optics that includes realistic models for the effects of profile defects and shows extremely good agreement with measured data and therefore the capability to predict performance in new geometries.
- Measured polycapillary fiber transmission in excess of 65% at 20 keV for borosilicate glass and in excess of 50% for lead glass. Measured high angle transmission (which corresponds to scatter transmission) is lower than 1% for 12 cm long borosilicate glass optics and 1 cm long lead glass optics.
- Modeling, measurement and defect studies have led to better manufacturing capabilities for magnifying tapered monolithic optics. These optics have demonstrated the ability to provide nearly ideal contrast enhancement, while at the same time increasing the system MTF performance at all spatial frequencies. A multitaper optic has been produced and tested.
- Image analysis studies have provided the means for image artifact analysis and reduction.

8. Reportable Outcomes

8.1. Manuscripts

Lei Wang, C. A. MacDonald, and W. W. Peppler, "Performance of Polycapillary Optics for Hard X-ray Imaging," accepted, Medical Physics.

Lei Wang, W.M. Gibson, C.A. MacDonald, "Potential of Polycapillary X-Ray Optics in Medical Imaging Applications," in C.A. MacDonald, K.A. Goldberg, J.R. Maldonado, A.J. Marker III, S.P. Vernon, eds., **EUV, X-ray, and Neutron Optics and Sources**, SPIE vol. 3767, 1999.

S.D. Padiyar, M.V. Gubarev, Hui Wang, W.M. Gibson, C.A. MacDonald "Characterization of Polycapillary X-Ray Collimating Optics", in C.A. MacDonald, K.A. Goldberg, J.R. Maldonado, A.J. Marker III, S.P. Vernon, eds., **EUV, X-ray, and Neutron Optics and Sources**, SPIE vol. 3767, 1999.

S.D. Padiyar, H. Wang, W.M. Gibson, C.A. MacDonald, M.V. Gubarev, "Beam Collimation Using Polycapillary X-Ray Optics For Large Area Diffraction Applications," in **Advances in X-ray Analysis**, 43, Proceedings of the 48th Denver X-ray Conference, 1999.

Hui Wang, Lei Wang, W.M. Gibson, C.A. MacDonald, "Simulation Study of Polycapillary X-Ray Optics," in **X-Ray Optics, Instruments, and Missions**, R.B. Hoover and A.B.C. Walker II, eds. SPIE Vol 3444, pp. 643-651, July 1998.

B.K. Rath, W.M. Gibson, Lei Wang, B.E. Homan and C.A. MacDonald, "Measurement and Analysis of Radiation Effects in Polycapillary X-ray Optics," Journal of Applied Physics, 83, no.12, pp. 7424-7435, June 15 1998.

8.2. Presentations

Lei Wang, W.M. Gibson, C.A. MacDonald, "Potential of Polycapillary X-Ray Optics in Medical Imaging Applications," SPIE 1999.

8.3. Poster Presentations

Hui Wang, Lei Wang, W.M. Gibson, C.A. MacDonald, "Simulation Study of Polycapillary X-ray Optics," SPIE San Diego 7/98.

8.4. Employment/Research Received

8.4.1. RESEARCH EMPLOYMENT

Lei Wang, Postdoctoral Residency, University of California at San Francisco, 1999.

9. Conclusions

Some manufacturing problems have occurred with scaling up the optics to clinical size. These problems have been addressed by the studies of defect properties. Notwithstanding the problems, the optics tested have performed extremely well. Multifiber collimating optics and monolithic linear magnifying tapers are being studied. Scatter rejection is very high from all the optics. The linear tapers resulted in nearly ideal contrast enhancements and simultaneously increase in MTF at all spatial frequencies. This will result in an improvement in resolution regardless the inherent spatial resolution of the detector. The rapidly growing modeling capability has lead to a real development of understanding of the nature of polycapillary defects, which is already leading to improvements in the manufacturing processes. Further, the increased confidence in the modeling allows future lens geometries to be effectively "tested" in simulation so that design parameters can be rapidly optimized.

10. References

- ¹ M.A. Kumakhov, F.F. Komarov, "Multiple Reflection from Surface X-Ray Optics," *Physics Reports*, **191**, (5): p. 289-350, 1990.
- ² W. M. Gibson, C. A. MacDonald and M. A. Kumakhov, "The Kumakhov Lens: A New X-ray and Neutron Optics with Potential for Medical Applications", in **Technology Requirements for Biomedical Imaging**, (ed. S. K. Mun, R. von Hanwehr and P. Gerity), IEEE Proc. 2580, 164-169 (1991).
- ³ J.F. Butler, F.P. Doty, B. Apotovsky, J. Lajzerowicz and L. Verger, "Gamma-and-X-ray detectors manufactured from $\text{Cd}_{1-x}\text{Zn}_x\text{Te}$ grown by a high pressure Bridgman method", *Materials Science & Engineering*, B16, 291 (1993).
- ⁴ M. Singh, F.P. Doty, S.J. Friesenhahn, J.F. Butler, "Feasibility of using cadmium-zinc-telluride detectors in electronically collimated SPECT." (Selected papers from the 1994 Nuclear Science Symposium and Medical Imaging Conference (NSS/MIC)), *IEEE Transactions on Nuclear Science*, August 1995, v42, n4, p1139(8).
- ⁵ Carman Abreu, "Investigation of Capillary Optics for Potential Use in Mammography", thesis for Ph.D. in physics, University at Albany, 1994.
- ⁶ David G. Kruger, Carmen C. Abreu, Eric G. Hendee, Armen Kocharian, Walter W. Peppler, Charles A. Mistretta and Carolyn A. MacDonald, "Imaging characteristics of x-ray capillary optics in digital mammography," *Medical physics*, Vol. 23, No. 2, Feb. 1996, pp 187-196.
- ⁷ Q.F. Xiao, I.Y. Ponamarev, A.I. Kolomitsev and J.C. Kimball, in R.B. Hoover, ed., **X-ray Detector Physics and Applications**, SPIE 1992.
- ⁸ B.L. Henke, E.M. Gullikson, and J.C. Davis, *Atomic Data and Nuclear Data Tables*, **54** (2), p. 181, 1993.
- ⁹ Lei Wang, B.K. Rath, W.M. Gibson, J.C. Kimball, C.A. MacDonald, "Measurement and Analysis of Capillary Optic Performance for Hard X rays," *Jour. Appl. Phys.*, September 15, 1996.
- ¹⁰ Hui Wang, Lei Wang, W.M. Gibson, C.A. MacDonald, "Simulation Study of Polycapillary X-Ray Optics," in SPIE Vol 3444, July 1998.
- ¹¹ Lei Wang and C.A. MacDonald, "Measurement of Capillary Optic Performance for Hard X rays," in R.B. Hoover and M.B. Williams, **X-ray and Ultraviolet Sensors and Applications**, SPIE vol. 2519, July 1995.
- ¹² Lei Wang and C.A. MacDonald, "Measurement and analysis of capillary optic performance for hard x-rays", **Hard X-ray/Gamma-Ray and Neutron Optics, Sensors, and Applications**, R.B. Hoover, and F.P. Doty, eds., SPIE Proceedings Vol. 2859.

¹³ J.C. Kimball and D. Bittel, "Surface Roughness and Scattering of glancing angle x-rays: Applications to X-ray lenses" J. Appl. Phys, **74 (2)**, 15 July 1993.

¹⁴ C. E. Dick and J. W. Motz, "New method for experimental evaluation of x-ray grids", Medical Physics, Vol. 5, No. 2, Mar./Apr. 1978.

¹⁵ Qin-sheng Chen, Michel Defrise, and F. Deconinck, "Symmetric Phase-Only Matched Filtering of Fourier-Mellin Transforms for Image Registration and Recognition", IEEE Transactions on Pattern Analysis and Machine Intelligence, Vol. 16, No. 12, December, pp. 1156.

¹⁶ Hiroshi Fujita, et. al. "A Simple Method for Determining the Modulation Transfer Function in Digital Radiography", IEEE Transaction on Medical Imaging, Vol. 11, No. 1, pp. 34.

¹⁷ Ehsan Samei, Michael J. Flynn, David A. Reimann, "A Method for Measureing the Presampled MTF of Digital Radiographic Systems using an Edge Test Device", manuscript submitted to Medical Physics, 1996.

¹⁸ John M. Boone and Seibert, "An analytical edge spread function model for computer fitting and subsequent calculation of the LSF and MTF", Medical Physics, Vol. 21, No. 10. October 1994., pp.1541